

The nucleon sigma term from lattice QCD

Rajan Gupta,^{1,*} Sungwoo Park,^{1,2,†} Martin Hoferichter,^{3,‡} Emanuele Mereghetti,^{1,§} Boram Yoon,^{4,¶} and Tanmoy Bhattacharya^{1,**}

¹*Los Alamos National Laboratory, Theoretical Division T-2, Los Alamos, NM 87545, USA*

²*Center for Nonlinear Studies, Los Alamos National Laboratory, Los Alamos, New Mexico 87545, USA*

³*Albert Einstein Center for Fundamental Physics, Institute for Theoretical Physics, University of Bern, Sidlerstrasse 5, 3012 Bern, Switzerland*

⁴*Los Alamos National Laboratory, Computer, Computational and Statistical Sciences Division CCS-7, Los Alamos, NM 87545, USA*

We present an analysis of the pion–nucleon σ -term, $\sigma_{\pi N}$, using six ensembles with 2+1+1-flavor highly improved staggered quark action generated by the MILC collaboration. The most serious systematic effect in lattice calculations of nucleon correlation functions is the contribution of excited states. We estimate these using chiral perturbation theory (χ PT), and show that the leading contribution to the isoscalar scalar charge comes from $N\pi$ and $N\pi\pi$ states. Therefore, we carry out two analyses of lattice data to remove excited-state contamination, the standard one and a new one including $N\pi$ and $N\pi\pi$ states. We find that the standard analysis gives $\sigma_{\pi N} = 40.4(4.7)$ MeV, consistent with previous lattice calculations, while the χ PT-motivated analysis gives $\sigma_{\pi N} = 61.6(6.4)$ MeV, which is consistent with phenomenological values obtained using πN scattering data. Our data on one physical pion mass ensemble was crucial for exposing this difference, therefore, calculations on additional physical mass ensembles are needed to confirm our result and resolve the tension between lattice QCD and phenomenology.

I. INTRODUCTION

This paper presents results for the pion–nucleon σ -term, $\sigma_{\pi N} \equiv m_{ud} g_S^{u+d} \equiv m_{ud} \langle N(\mathbf{k}, s) | \bar{u}u + \bar{d}d | N(\mathbf{k}, s) \rangle$ calculated in the isospin symmetric limit with $m_{ud} = (m_u + m_d)/2$ the average of the light quark masses. It is a fundamental parameter of QCD that quantifies the amount of the nucleon mass generated by the u - and d -quarks. It is determined on the lattice from the forward matrix element of the scalar density $\bar{q}q$ between the nucleon state, i.e., the scalar charge g_S^q defined by

$$g_S^q = \langle N(\mathbf{k} = 0, s) | Z_S \bar{q}q | N(\mathbf{k} = 0, s) \rangle, \quad (1)$$

where Z_S is the renormalization constant and the nucleon spinor has unit normalization. The connection between g_S^q and the rate of variation of the nucleon mass, M_N , with the quark mass is given by the Feynman–Hellmann (FH) relation [1–3]

$$\frac{\partial M_N}{\partial m_q} = \langle N(\mathbf{k}, s) | \bar{q}q | N(\mathbf{k}, s) \rangle = g_S^q / Z_S. \quad (2)$$

The charge, g_S^q , determines the coupling of the nucleon to the scalar quark current with flavor q —an important input quantity in the search for physics beyond the Standard Model (SM), including in direct-detection searches for dark matter [4–8], lepton flavor violation in

$\mu \rightarrow e$ conversion in nuclei [9, 10], and electric dipole moments [11–14]. In particular, $\sigma_{\pi N}$ is a rare example of a matrix element that, despite the lack of scalar probes in the SM, can still be extracted from phenomenology—via the Cheng–Dashen low-energy theorem [15, 16]—and thus defines an important benchmark quantity for lattice QCD.

The low-energy theorem establishes a connection between $\sigma_{\pi N}$ and a pion–nucleon (πN) scattering amplitude, albeit evaluated at unphysical kinematics. With one-loop corrections free of chiral logarithms [17, 18], the remaining corrections to the low-energy theorem scale as $\sigma_{\pi N} M_\pi^2 / M_N^2 \approx 1$ MeV, leaving the challenge of controlling the analytic continuation of the πN amplitude. Stabilizing this extrapolation by means of dispersion relations, Refs. [19–21] found $\sigma_{\pi N} \approx 45$ MeV based on the partial-wave analyses from Refs. [22, 23]. More recent partial-wave analyses [24, 25] favor higher values, e.g., $\sigma_{\pi N} = 64(8)$ MeV [26]. Similarly, χ PT analyses depend crucially on the πN input, with σ -term prediction varying accordingly [27, 28].

The analytic continuation can be further improved in the framework of Roy–Steiner equations [29–37], whose constraints on $\sigma_{\pi N}$ become most powerful when combined with pionic-atom data on threshold πN scattering [38–42]. Slightly updating the result from Refs. [31, 33] to account for the latest data on the pionic hydrogen width [40], one finds $\sigma_{\pi N} = 59.0(3.5)$ MeV. In particular, this determination includes isospin-breaking corrections [43–46] to ensure that $\sigma_{\pi N}$ coincides with its definition in lattice QCD calculations [34]. The difference to Refs. [19–21] traces back to the scattering lengths implied by Refs. [22, 23], which are incompatible with the modern pionic-atom data. Independent constraints from experiment are provided by low-energy πN cross

* rajan@lanl.gov

† sungwoo@lanl.gov

‡ hoferichter@itp.unibe.ch

§ emereghetti@lanl.gov

¶ boram@lanl.gov

** tanmoy@lanl.gov

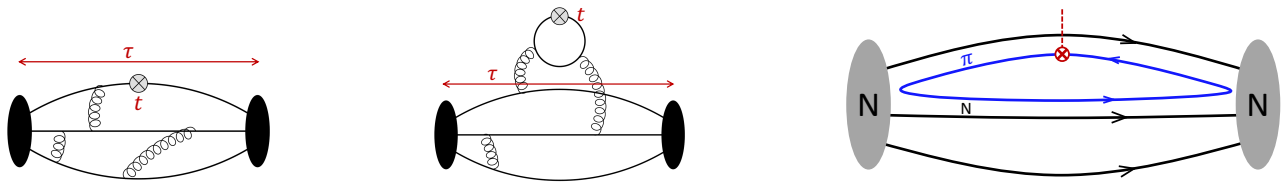


FIG. 1. The connected (left) and disconnected ((middle) and redrawn to highlight the $N\pi$ intermediate state (right)) diagrams contributing to the 3-point function that determines the flavor-diagonal matrix elements of the scalar operator (shown by \otimes at time slice t) within the nucleon state. The black blobs denote nucleon source and sink, separated by Euclidean time τ .

sections, including more recent data on both the elastic reactions [47–49] and the charge exchange [50–53], and a global analysis of low-energy data in the Roy–Steiner framework leads to $\sigma_{\pi N} = 58(5) \text{ MeV}$ [37], in perfect agreement with the pionic-atom result. In contrast, so far lattice QCD calculations [54–62] have favored low values $\sigma_{\pi N} \approx 40 \text{ MeV}$ (with the exception of Ref. [63]), and it is this persistent tension with phenomenology that we aim to address in this paper.

There are two ways to calculate $\sigma_{\pi N}$ using lattice QCD, which are called the FH and the direct methods [64]. In the FH method, the nucleon mass is obtained as a function of the bare quark mass m_{ud} (equivalently M_π^2) from the nucleon 2-point correlation function, and its numerical derivative multiplied by m_{ud} gives $\sigma_{\pi N}$. In the direct method, the matrix element of $\bar{u}u + \bar{d}d$ is calculated within the ground-state nucleon. Both methods have their challenges. In the FH method, one needs to calculate the derivative about the physical m_{ud} , which is computationally very demanding. Most calculations extrapolate from heavier masses or fit the data for M_N versus M_π^2 to an ansatz motivated by χ PT and evaluate its derivative at m_{ud} . The signal in the direct method is noisier since it involves a 3-point function with the insertion of the scalar density, and one has to ensure that all excited-states contamination (ESC) has been removed. Estimates from both methods give $\sigma_{\pi N} \approx 40 \text{ MeV}$, as reviewed by the Flavour Lattice Averaging Group (FLAG) in 2019 [64] and since presented in Refs. [61, 62].

In this paper, we present a new direct-method calculation. Our main message is that $N\pi$ and $N\pi\pi$ excited states, which have not been included in previous lattice calculations, can make a significant contribution. We provide motivation for this effect from heavy-baryon χ PT [65, 66], and show that including the excited states in fits to the spectral decomposition of the 3-point function increases the result by about 50%. Such a change brings the lattice result in agreement with the phenomenological value.

II. LATTICE METHODOLOGY AND EXCITED STATES

The construction of all nucleon 2- and 3-point correlations functions is carried out using Wilson-clover fermions on six 2+1+1-flavor ensembles generated using

the highly improved staggered quark (HISQ) action [67] by the MILC collaboration [68]. In each of these ensembles, the u - and d -quark masses are degenerate, and the s - and c -quark masses have been tuned to their physical values. The six ensembles are at three values of the lattice spacing, $a \approx 0.12, 0.09$, and 0.06 fm , and three values of $M_\pi \approx 315, 230$, and 138 MeV . The physical pion mass ensemble is labeled $a09m130$. Details of lattice parameters are given in Table I (and Table II in App. A). To obtain flavor-diagonal charges g_S^q , two kinds of diagrams, called connected and disconnected (illustrated in Fig. 1), need to be calculated. The details of the methodology for the calculation of the connected contributions (isovector charges) using this clover-on-HISQ formulation are given in Refs. [69, 70] and of the disconnected ones in Ref. [69].

The main focus of the analysis is on controlling the ESC. To this end, we estimate $\sigma_{\pi N}$ using two possible sets of excited-state masses, M_1 and M_2 , given in Table I. These M_i are obtained by fitting the data for the zero momentum nucleon 2-point function, $C^{2\text{pt}}$, and then enter in fits to the 3-point function $C^{3\text{pt}}$. The two fits are made using the spectral decomposition truncated to four and three states respectively:

$$C^{2\text{pt}}(\tau; \mathbf{k}) = \sum_{i=0}^3 |\mathcal{A}_i(\mathbf{k})|^2 e^{-M_i \tau},$$

$$C_S^{3\text{pt}}(\tau; t) = \sum_{i,j=0}^2 \mathcal{A}_i \mathcal{A}_j^* \langle i | \mathcal{S} | j \rangle e^{-M_i t - M_j (\tau - t)}. \quad (3)$$

Here \mathcal{A}_i are the amplitudes for the creation/annihilation of states by the nucleon interpolating operator used on the lattice, $\mathcal{N} = \epsilon^{abc} [u^{aT} C \gamma_5 (1 + \gamma_4) d^b] u^c$, with color indices $\{a, b, c\}$ and charge conjugation matrix C . The nucleon source–sink separation is labeled by τ and the operator insertion time by t .

The issue of ESC arises because \mathcal{N} couples not only to the ground-state nucleon but to all its excitations including multihadron states with the same quantum numbers. In the current data, the signal in $C_S^{3\text{pt}}$ extends to $\tau \approx 1.5 \text{ fm}$, at which source–sink separation the contribution of excited states is significant as evident from the dependence on $\{\tau, t\}$ in the ratio $\mathcal{R}_S(\tau, t) = C_S^{3\text{pt}}(t, \tau) / C^{2\text{pt}}(\tau)$ shown in Fig. 2. In the limits $t \rightarrow \infty$ and $(\tau - t) \rightarrow \infty$, the ratio $\mathcal{R}_S(\tau, t) \rightarrow g_S$. The key parameters in the fits to $C^{3\text{pt}}$ using Eq. (3) are the number of excited states that should be kept and their masses M_i . Fits to $C^{3\text{pt}}$ with

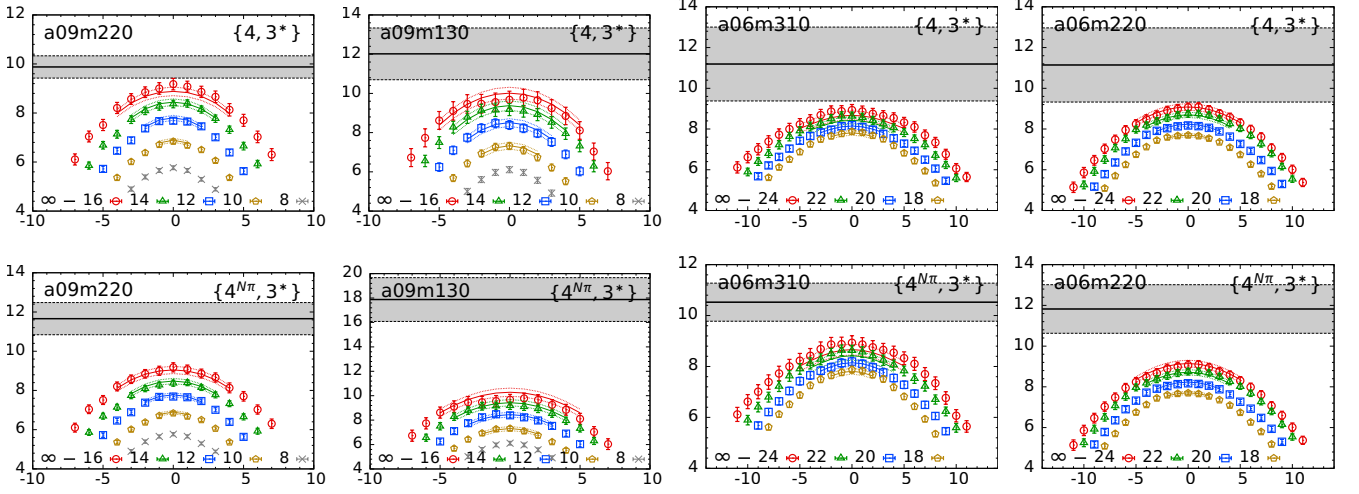


FIG. 2. Results of the $\{4, 3^*\}$ (top row) and $\{4^{N\pi}, 3^*\}$ (bottom row) fits to the sum of the connected and disconnected data plotted versus $(t - \tau/2)/a$ for ensembles $a09m220$, $a09m130$, $a06m310$, and $a06m220$. Result of the fit is shown by lines of the same color as the data for various τ/a listed in the label, and the $\tau = \infty$ value is given by the gray band.

Ensemble ID	m_{ud}^{bare} (MeV)	$\{4, 3^*\}$					$\{4^{N\pi}, 3^*\}$				
		M_1 (GeV)	M_2 (GeV)	χ^2/dof	$g_S^{u+d, \text{bare}}$	$\sigma_{\pi N}$ (MeV)	M_1 (GeV)	M_2 (GeV)	χ^2/dof	$g_S^{u+d, \text{bare}}$	$\sigma_{\pi N}$ (MeV)
a12m310	18.71(53)	1.71(06)	1.95(13)	14.9/19	8.26(33)	154.6(7.6)	1.69(02)	1.96(11)	14.9/19	8.27(32)	154.7(7.4)
a12m220	9.91(51)	1.52(14)	2.23(13)	25.7/19	11.9(1.9)	118(20)	1.46(03)	2.18(12)	26.0/19	11.84(87)	117(11)
a09m220	9.35(12)	1.80(09)	1.95(14)	20.8/19	9.88(45)	92.4(4.4)	1.46(02)	1.79(08)	20.8/19	11.66(82)	109.0(7.8)
a09m130	3.47(09)	1.58(11)	2.08(16)	26.5/27	12.0(1.3)	41.7(4.7)	1.22(02)	1.63(10)	29.6/27	17.9(1.8)	62.1(6.4)
a06m310	17.20(15)	1.66(15)	2.39(14)	22.9/27	11.2(1.8)	192(31)	1.70(08)	2.38(15)	23.1/27	10.52(75)	181(13)
a06m220	9.05(11)	1.72(12)	2.18(17)	21.2/27	11.1(1.8)	101(17)	1.61(10)	1.93(15)	20.9/27	11.8(1.2)	107(11)

TABLE I. The excited-state masses, M_1 and M_2 , χ^2/dof of the fit, and the resulting value of the bare isoscalar charge and $\sigma_{\pi N}$ with the two strategies $\{4, 3^*\}$ and $\{4^{N\pi}, 3^*\}$. The second column gives the bare quark mass m_{ud}^{bare} .

the M_i left as free parameters have large fluctuations. We, therefore, remove ESC and extract the ground-state matrix element, $\langle 0|S|0\rangle$, by using the M_i from $C^{2\text{pt}}$ because, in principle, the set of M_i should be the same in $C^{2\text{pt}}$ and $C^{3\text{pt}}$. On the other hand, their contribution depends on the operator inserted even though the same N is used in both. That this happens for many matrix elements has been discussed in detail in Refs. [71, 72], in particular for the axial-vector form factors, where the $N\pi$ state gives a large contribution. Thus, our operational strategy is the following: we use the statistical precision of the data for $C^{2\text{pt}}$ and $C^{3\text{pt}}$ to determine how many states are retained without overparameterization, and calculate $\sigma_{\pi N}$ for two plausible but significantly different values of M_1 and M_2 that give fits with similar χ^2 .

Data for $C^{3\text{pt}}$, by Eq. (3), should be (i) symmetric about $\tau/2$, and (ii) converge monotonically in τ for sufficiently large τ , especially when a single excited state dominates. These two conditions are, within errors, satisfied by the data shown in Fig. 2 (and Fig. 6 in App. B) and allow us to make, without overparameterization, fits with two excited states. These are called $\{3^*\}$ since we set the $\langle 2|S|2\rangle$ term in Eq. (3) to zero as it is not re-

solved, and are specified by the two masses M_1 and M_2 . We can, in principle, obtain these M_i from 4-state fits to $C^{2\text{pt}}$, however, as discussed in Refs. [70, 72], the data are not precise enough for that. We find a large region in $M_{i>0}$ in which the augmented χ^2 of fits with priors for M_i is essentially the same, i.e., many M_i are plausible. Theoretically, there are towers of positive parity $N\pi$, $N\pi\pi$, ..., multihadron states labeled by increasing relative momentum \mathbf{k} that can contribute, and these start at energies smaller than those of radial excitations. To obtain guidance on which excited states give large contributions to $C^{3\text{pt}}$, we carried out a χPT analysis.

This approach leads us to study two well-motivated values of M_1 and M_2 for the analysis of $C^{3\text{pt}}$, both obtained from $C^{2\text{pt}}$. The “standard” strategy (called the $\{4\}$ fit) takes the spectrum from a fit to the 2-point function without imposing narrow priors, while the $\{4^{N\pi}\}$ fit uses a narrow-width prior for M_1 centered about the noninteracting energy of the lowest positive parity states $N(\mathbf{1})\pi(-\mathbf{1})$ or $N(\mathbf{0})\pi(\mathbf{0})\pi(\mathbf{0})$, which have similar energies for our ensembles. Thus, when using the label $N\pi$ we imply that the contribution of both states is included. Details of getting the M_i from these two four-state fits,

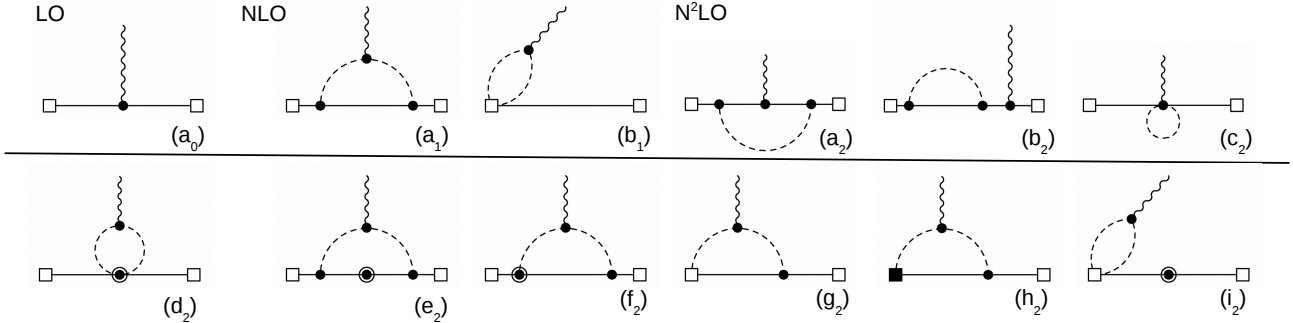


FIG. 3. Corrections to the scalar charge in χ PT. An empty and full square denote, respectively, an insertion of the leading-order (LO) and NLO expansion of the source fields \mathcal{N} and $\bar{\mathcal{N}}$. Plain, dashed, and wavy lines denote, respectively, nucleons, pions, and an insertion of the scalar source. Dots and circled dots denote LO and NLO vertices in the chiral Lagrangian. We show one diagram for each topology, and the inclusion of all the possible orderings is understood. Diagrams (g_2) , (h_2) , and (i_2) are representative of N²LO corrections arising from the chiral expansion of \mathcal{N} . We do not consider these diagrams in our calculation, as they only produce N²LO recoil corrections (including (g_2) despite containing only LO interactions [73, 74]).

$\{4\}$ and $\{4^{N\pi}\}$, to $C^{2\text{pt}}$ can be found in Ref. [72]. For the $a09m130$ ensemble with $M_\pi = 138$ MeV, the $\{M_1, M_2\}$ are $\{1.58, 2.08\}$ and $\{1.22, 1.63\}$ GeV for the two cases, as shown in Table I. Using these as input, we find that the χ^2 of the $\{3^*\}$ fits to $C^{3\text{pt}}$ are equally good, however, the results for the isoscalar charge g_S^{u+d} differ significantly.

The $\{4, 3^*\}$ fit leads to a result consistent with $\sigma_{\pi N} \approx 40$ MeV, whereas the $\{4^{N\pi}, 3^*\}$ fit gives ≈ 60 MeV. The major difference comes from the disconnected quark loop diagram shown in Fig. 1, and is strongly M_π dependent—the effect of these $N\pi$ states is hard to resolve in the $M_\pi \approx 315$ MeV data, debatable in the 230 MeV data, and clear in the $M_\pi = 138$ MeV data.

It is important to point out that the values of M_1 and M_2 used in both fit strategies are an effective bundling of the many excited states that contribute into two. In fact, as mentioned above, many combinations of M_1 and M_2 between the two cases used (see Table I) give fits with equally good χ^2 values. In Ref. [72], we showed that for $\tau \gtrsim 1.0$ fm and for both fit strategies, the dominant ESC in $C^{3\text{pt}}$ comes from the first excited state. Thus, operationally, our two results for $\sigma_{\pi N}$ should be regarded as: what happens if the first “effective” excited state has $M_1 \approx 1220$ MeV (motivated by χ PT and corresponding to the lowest theoretically possible states $N\pi$ or $N\pi\pi$) versus 1600 MeV (obtained from the standard fit to the 2-point function and taken as an upper limit on M_1)? To further resolve all the excited states that contribute significantly and their energy levels in a finite box will require much higher precision data on additional physical pion mass ensembles. In short, while our $\{4^{N\pi}, 3^*\}$ analysis reconciles the lattice and the phenomenological values, it also calls for validation in future calculations.

III. EXCITED STATES IN χ PT

The contributions of low-momentum $N\pi$ and $N\pi\pi$ excitations to the lattice 2- and 3-point functions $C^{2\text{pt}}$ and $C^{3\text{pt}}$ can be studied in χ PT [73–80], a low-energy effective field theory (EFT) of QCD that provides a systematic expansion of $\mathcal{R}_S(\tau, t)$ in powers of Q/Λ_χ , where Q denotes a low-energy scale of order of the pion mass, $Q \in \{M_\pi, t^{-1}, (\tau - t)^{-1}\}$, while $\Lambda_\chi \approx 1$ GeV is the typical scale of QCD. In contrast to the isovector scalar charge considered in Ref. [75], we find large contributions from the $N(\mathbf{k})\pi(-\mathbf{k})$ and $N(\mathbf{0})\pi(\mathbf{k})\pi(-\mathbf{k})$ states, which can give up to 30% corrections to \mathcal{R}_S and thus affect the extraction of g_S^{u+d} and $\sigma_{\pi N}$ in a significant way. Details of this calculation at next-to-next-to-leading order (N²LO) in χ PT are given in App. B.

The diagrams contributing to \mathcal{R}_S are shown in Fig. 3, where we assume $\mathcal{N}(x)$ to be a local nucleon source with well defined transformation properties under chiral symmetry. The chiral representation of this class of sources has been derived in Ref. [73, 74, 81], and the expansion of \mathcal{N} in terms of heavy nucleon and pion fields is summarized in App. B. The crucial observation is that the isoscalar scalar source couples strongly to two pions, so that loop diagrams with the scalar source emitting two pions, which are consequently absorbed by the nucleon, are suppressed by only one chiral order, Q/Λ_χ . These diagrams have both $N\pi$ and $N\pi\pi$ cuts, which give rise to ESC to Euclidean Green’s functions. A second important effect is that the next-to-leading-order (NLO) couplings of the nucleon to two pions, parameterized in χ PT by the low-energy constants (LECs) $c_{1,2,3}$, are sizable, reflecting the enhancement by degrees of freedom related to the $\Delta(1232)$. When the pions couple to the isoscalar source, these couplings give rise to large N²LO corrections that are dominated by $N\pi\pi$ excited states and have the same sign as the NLO correction. Since, in

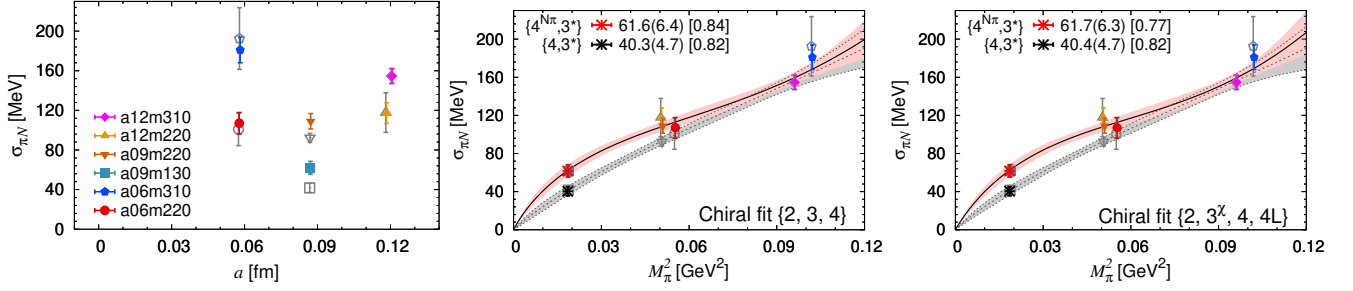


FIG. 4. Data for the σ -term, $\sigma_{\pi N} = m_{ud}g_S^{u+d}$, from the two ESC strategies $\{4, 3^*\}$ (gray) and $\{4^{N\pi}, 3^*\}$ (color) are shown as a function of a (left) and M_π^2 , including two chiral fits $\{2, 3, 4\}$ (middle) and $\{2, 3^x, 4, 4L\}$ (right) described in the text. The result at $M_\pi = 135$ MeV and $[\chi^2/\text{dof}]$ from the two fits are given in the legend.

the isospin-symmetric limit, the isovector scalar source does not couple to two pions, the NLO diagrams and the N²LO diagrams proportional to $c_{1,2,3}$ do not contribute to the isovector 3-point function, whose leading ESC arises at $\mathcal{O}(Q^2/\Lambda_\chi^2)$. A detailed analysis showing that the functional form of the ESC predicted by χ PT matches the lattice data and fits for sufficiently large time separations τ is given in App. B. In particular, the NLO and N²LO ESC can each reduce $\sigma_{\pi N}$ at a level of 10 MeV, thus explaining the $\{4^{N\pi}, 3^*\}$ fits, i.e., when ESC is taken into account.

IV. ANALYSIS OF LATTICE DATA

Examples of the fits with the two strategies $\{4, 3^*\}$ and $\{4^{N\pi}, 3^*\}$ are shown in Fig. 2 and the results summarized in Table I. The final results are obtained from fits to the sum of the connected and disconnected contributions. To investigate the source of the disagreement in results between the two ESC strategies, we also made separate fits to $g_S^{u+d, \text{conn}}$ and g_S^{2l} and added the results. The two sets of estimates overlap in all cases. From the separate fits, we infer that the main difference between the two ESC strategies comes from the disconnected diagrams, which we interpret as due to the $N\pi/N\pi\pi$ contributions through quark-level diagrams such as in Fig. 1 (right).

The data for $\sigma_{\pi N} = m_{ud}^{\text{bare}} g_S^{u+d, \text{bare}}$ are shown in Fig. 4 as a function of a and M_π^2 . The bare quark mass is defined to be $m_{ud}^{\text{bare}} = 1/2\kappa_l - 1/2\kappa_c$, with the critical value of the hopping parameter, κ_c , determined using a linear fit to $(aM_\pi)^2$ versus $1/2\kappa$ at each of the three values of a . No renormalization is needed since $\sigma_{\pi N}$ is renormalization scheme and scale independent. The data in Fig. 4 show no clear dependence on a , so we neglect it in this work, as well as possible finite-volume corrections, which are observed to be small in related quantities [70, 82].

Figure 4 also shows two chiral fits based on the N²LO χ PT expression for $\sigma_{\pi N}$. The $\{2, 3, 4\}$ fit corresponds to keeping terms proportional to $\{M_\pi^2, M_\pi^3, M_\pi^4\}$ with all coefficients free. The $\{2, 3^x, 4, 4L\}$ fit keeps $\{M_\pi^2, M_\pi^3, M_\pi^4, M_\pi^4 \log M_\pi^2\}$ terms with the coefficient of the M_π^3 term, which does not involve any LECs, fixed to the χ PT prediction. Our six data points are at only

three values of M_π^2 , so the result of both fits at the physical point $M_\pi = 135$ MeV are essentially given by the $a09m130$ ensemble point. For our final result, we take the average of results from these two fits to the $\{4^{N\pi}, 3^*\}$ data, which overlap. In App. B we also consider more constrained fit variants, which show that the fit coefficients of the M_π^2 and $M_\pi^4 \log M_\pi^2$ terms are fully consistent with their χ PT prediction as well.

V. CONCLUSIONS

Results for $\sigma_{\pi N}$ were reviewed by FLAG in 2019 [64], and there have been two new calculations since as summarized in App. C. The ETM collaboration [61], using the direct method on one physical mass 2+1+1-flavor twisted mass clover-improved ensemble, obtained $\sigma_{\pi N} = 41.6(3.8)$ MeV; the BMW collaboration using the FH method and 33 ensembles of 1+1+1+1-flavor Wilson-clover fermions [62], but all with $M_\pi > 199$ MeV, find $\sigma_{\pi N} = 37.4(5.1)$ MeV. The χ PT analysis of the impact of low-lying excited $N\pi$ states in the FH and direct methods is the same, and as shown in Fig. 4, it mainly affects the behavior for $M_\pi \lesssim 135$ MeV. Our work indicates that previous lattice calculations give the lower value $\sigma_{\pi N} \approx 40$ MeV because in the FH analysis [62] the fit ansatz (Taylor/Padé) parameters are determined using $M_\pi \geq 199$ MeV data, and in the direct method, the $N\pi/N\pi\pi$ states have not been included when extracting the ground-state matrix element.

To conclude, a χ PT analysis shows that the low-lying $N\pi$ and $N\pi\pi$ states can make a significant contribution to g_S^{u+d} . Including these states in our analysis (the $\{4^{N\pi}, 3^*\}$ strategy) gives $\sigma_{\pi N} = 61.6(6.4)$ MeV, whereas the standard analysis ($\{4, 3^*\}$ strategy) gives $\sigma_{\pi N} = 40.4(4.7)$ MeV consistent with previous analyses [64]. These chiral fits are shown in Fig. 4. Since the $\{4, 3^*\}$ and $\{4^{N\pi}, 3^*\}$ strategies are not distinguished by the χ^2 of the fits, we have provided a detailed N²LO χ PT analysis of ESC, which reveals sizable corrections consistent with the $\{4^{N\pi}, 3^*\}$ analysis, restoring agreement with phenomenology. Since the effect of the $N\pi$ and $N\pi\pi$ states becomes significant near $M_\pi = 135$ MeV, further work on physical mass ensembles is needed to

Ensemble ID	a (fm)	M_π (MeV)	$(L/a)^3 \times T/a$	$M_\pi L$	$N_{\text{conf}}^{\text{conn}}$	N_{LP}	N_{HP}	N_{conf}^l	N_{src}^l	$N_{\text{LP}}^l/N_{\text{HP}}^l$
$a12m310$	0.1207(11)	310(3)	$24^3 \times 64$	4.55	1013	64	8	1013	5000	30
$a12m220$	0.1184(10)	228(2)	$32^3 \times 64$	4.38	744	64	4	958	11000	30
$a09m220$	0.0872(07)	226(2)	$48^3 \times 96$	4.79	964	128	8	712	8000	30
$a09m130$	0.0871(06)	138(1)	$64^3 \times 96$	3.90	1290	128	4	1270	10000	50
$a06m310$	0.0582(04)	320(2)	$48^3 \times 144$	4.52	500	128	4	830	12000	50
$a06m220$	0.0578(04)	235(2)	$64^3 \times 144$	4.41	649	64	4	1001	10000	50

TABLE II. Lattice parameters of the six ensembles analyzed for the isoscalar scalar charge g_S^{u+d} . Columns 6–8 give the number of configurations analyzed, and the number of low- (high-) precision measurements made per configuration for the connected contributions. Columns 9–11 give the number of configurations, low-precision random sources used, and the ratio $N_{\text{LP}}/N_{\text{HP}}$ for the disconnected contributions. The analysis of the isovector contributions has been presented in Ref. [70].

validate our result and to increase the precision in the extraction of the nucleon isoscalar scalar charge.

ACKNOWLEDGMENTS

We thank the MILC collaboration for providing the 2+1+1-flavor HISQ lattices. The calculations used the Chroma software suite [83]. This research used resources at (i) the National Energy Research Scientific Computing Center, a DOE Office of Science User Facility supported by the Office of Science of the U.S. Department of Energy under Contract No. DE-AC02-05CH11231; (ii) the Oak Ridge Leadership Computing Facility, which is a DOE Office of Science User Facility supported under Contract DE-AC05-00OR22725, and was awarded through the ALCC program project LGT107; (iii) the USQCD collaboration, which is funded by the Office of Science of the U.S. Department of Energy; and (iv) Institutional Computing at Los Alamos National Laboratory. T. Bhattacharya and R. Gupta were partly supported by the U.S. Department of Energy, Office of Science, Office of High Energy Physics under Contract No. DE-AC52-06NA25396. T. Bhattacharya, R. Gupta, E. Mereghetti, S. Park, and B. Yoon were partly supported by the LANL LDRD program, and S. Park by the Center for Nonlinear Studies. M. Hoferichter was supported by the Swiss National Science Foundation (Project No. PCEFP2_181117).

Appendix A: Lattice Parameters

The parameters of the six 2+1+1-flavor ensembles generated using the HISQ action [67] by the MILC collaboration [68] are given in Table II. On each of these ensembles, the calculations of the 2- and 3-point functions was carried out using tadpole improved Wilson-clover fermions as described in Ref. [70].

All correlators are constructed using the truncated solver method with bias correction [70, 84, 85]. In this

method, high statistics are obtained by using a low-precision (LP) stopping criterion in the inversion of the quark propagators, which was taken to be between $r_{\text{LP}} \equiv |\text{residue}|_{\text{LP}}/|\text{source}| = 10^{-3}$ and 5×10^{-4} . These estimates are corrected for possible bias using high-precision (HP) measurements with r_{HP} taken to be between 10^{-7} and 10^{-8} [69, 70]. The number of configurations analyzed, and the number of LP and HP measurements made for the connected and disconnected contributions, are given in Table II. In our data, the bias correction term was found to be a fraction of the error in all quantities and for all six ensembles.

To reduce ESC, the source used to generate quark propagators was smeared using the Wuppertal method [86]. The same smearing is used at the source and sink points and the smearing parameters are given in Ref. [70].

For the statistical analysis of the data, we first constructed bias-corrected values for the 2- and 3-point correlation functions, and then averaged these over the multiple measurements made on each configuration. Using these, we constructed 300 bootstrap samples, each consisting of 300 configuration-averaged values drawn randomly from the full sets.

Appendix B: Chiral Perturbation Theory

The corrections to the nucleon mass and the σ -term in χ PT have a long history in the literature [17, 18, 66, 87–97]. The LO, NLO, and N²LO diagrams contributing to the isoscalar scalar charge g_S^{u+d} have been shown in Fig. 3. In these diagrams, plain and dashed lines denote pions and nucleons in the interaction picture of χ PT, and not the nucleon and pion eigenstates of the full theory.

These diagrams lead to the expansion

$$g_S^{u+d} = g_S^{(0)} + g_S^{(1)} \frac{M_\pi}{\Lambda_\chi} + g_S^{(2)} \frac{M_\pi^2}{\Lambda_\chi^2} + \dots, \quad (\text{B1})$$

where $\Lambda_\chi = 4\pi F_\pi \approx 1$ GeV is the breakdown scale of the chiral expansion. The NLO diagrams (a_1) and (b_1) in

$ \mathbf{n}_{\max} $	$m_{\mathbf{n}}$	NLO		N ² LO		$\delta\sigma_{\pi N}(16, 8)$	NLO		N ² LO		$\delta\sigma_{\pi N}(12, 6)$
		loop	source	c_i	recoil	total	loop	source	c_i	recoil	total
0	1	0	-0.4	-1.0	-0.0	-1.4	0	-0.5	-1.2	-0.1	-1.7
1	6	-2.2	-0.6	-2.9	-0.2	-5.9	-2.7	-0.9	-4.3	-0.2	-8.0
$\sqrt{2}$	12	-4.4	-0.8	-4.6	-0.3	-10.0	-5.6	-1.2	-7.4	-0.3	-14.5
$\sqrt{3}$	8	-5.2	-0.8	-5.2	-0.3	-11.6	-6.7	-1.3	-8.7	-0.4	-17.1
2	6	-5.6	-0.9	-5.5	-0.3	-12.2	-7.3	-1.3	-9.4	-0.4	-18.4
$\sqrt{5}$	24	-6.5	-0.9	-6.2	-0.3	-14.0	-8.9	-1.4	-11.1	-0.5	-21.9
$\sqrt{6}$	24	-7.2	-0.9	-6.7	-0.4	-15.2	-10.1	-1.5	-12.4	-0.5	-24.5
$\sqrt{8}$	12	-7.4	-0.9	-6.8	-0.4	-15.5	-10.4	-1.5	-12.8	-0.5	-25.2
3	30	-7.7	-0.9	-7.0	-0.4	-16.0	-11.1	-1.6	-13.5	-0.5	-26.6
∞		-9.2	-0.9	-7.6	-0.4	-18.0	-14.2	-1.5	-16.3	-0.6	-32.6

TABLE III. Excited-state corrections to the σ -term (in MeV). $\delta\sigma_{\pi N}(\tau, t)$, defined in Eq. (B12), is evaluated for $t = \tau/2 = 8a$ (left) and $t = \tau/2 = 6a$ (right), using the parameters of the $a09m130$ lattice ensemble listed in Table II. $|\mathbf{n}_{\max}|$ denotes the maximum momentum included in the sum in Eqs. (B5), (B8), and (B9), $m_{\mathbf{n}}$ the multiplicity of the momentum state [98]. We split the NLO corrections in Eq. (B5) into the loop diagram (a_1) in Fig. 3, which also contributes to the ground state, and the diagram in which the scalar source couples to pions emitted by the nucleon source \mathcal{N} . At N²LO, we label by c_i the contributions in Eq. (B9) and by “recoil” those in Eq. (B8). The last line is evaluated in the continuum.

Fig. 3 only contribute to the isoscalar channel, implying that the isovector channel has the different expansion

$$g_S^{u-d} = \tilde{g}_S^{(0)} + \tilde{g}_S^{(2)} \frac{M_\pi^2}{\Lambda_\chi^2} + \dots \quad (\text{B2})$$

We will show that the same loop diagrams responsible for the NLO and N²LO corrections to g_S also induce a sizable contribution from $N\pi$ and $N\pi\pi$ intermediate states.

To this end, we calculate the ratio $\mathcal{R}_S(\tau, t)$ using heavy-baryon χ PT and expand it as

$$\mathcal{R}(\tau, t) = \mathcal{R}^{(0)}(\tau, t) + \mathcal{R}^{(1)}(\tau, t) + \mathcal{R}^{(2)}(\tau, t), \quad (\text{B3})$$

including in its definition a factor m_{ud} to make the result $\mathcal{R} = m_{ud}\mathcal{R}_S$ scale independent and ensure a normalization that facilitates the comparison to $\sigma_{\pi N}$. We assume \mathcal{N} to be a local nucleon source, transforming as $(\frac{1}{2}, 0) \oplus (0, \frac{1}{2})$ under the chiral group $SU(2)_L \otimes SU(2)_R$. The heavy-baryon χ PT realization of \mathcal{N} was constructed in Ref. [74]

$$\mathcal{N}(x) = \left[\left(1 - \frac{\pi^2}{8F_\pi^2} \right) - i \frac{\pi \cdot \tau}{2F_\pi} \gamma_5 \right] N_v + \mathcal{O}\left(\frac{1}{M_N}\right), \quad (\text{B4})$$

where $N_v = (1 + \gamma_4)/2N_v$ represents a heavy-nucleon field. At $\mathcal{O}(1/M_N)$, Eq. (B4) contains additional LECs, which reduce the predictive power of the calculation.

At LO one simply has $\mathcal{R}^{(0)} = m_{ud}g_S^{(0)}$. The NLO diagrams receive contributions from nucleon, $N\pi$, and $N\pi\pi$ excited states, leading to

$$\begin{aligned} \mathcal{R}^{(1)}(\tau, t) = & \frac{3g_A^2 M_\pi^2}{8F_\pi^2 L^3} \sum_{\mathbf{k}} \frac{\mathbf{k}^2}{E_\pi^4} \left[1 - e^{-E_{N\pi}t} - e^{-E_{N\pi}t_B} \right. \\ & \left. + \frac{1}{2}e^{-E_{N\pi}\tau} + \frac{1}{4}e^{-2E_\pi t} + \frac{1}{4}e^{-2E_\pi t_B} \right] \\ & - \frac{3M_\pi^2}{32F_\pi^2 L^3} \sum_{\mathbf{k}} \frac{1}{E_\pi^2} (e^{-2E_\pi t} + e^{-2E_\pi t_B}), \quad (\text{B5}) \end{aligned}$$

where $E_\pi = \sqrt{\mathbf{k}^2 + M_\pi^2}$, $\tilde{E}_N = \sqrt{M_N^2 + \mathbf{k}^2} - M_N$, $E_{N\pi} = E_\pi + \tilde{E}_N$, $\mathbf{k} = 2\pi\mathbf{n}/L$, and $t_B = \tau - t$. $F_\pi = 92.3 \text{ MeV}$ is the pion decay constant, $g_A = 1.276$ the axial charge of the nucleon [99]. The first term in Eq. (B5) is a correction to the ground-state contribution

$$\frac{3g_A^2 M_\pi^2}{8F_\pi^2 L^3} \sum_{\mathbf{k}} \frac{\mathbf{k}^2}{E_\pi^4} = -\frac{9g_A^2 M_\pi^3}{64\pi F_\pi^2} + \Delta_L \sigma_{\pi N}, \quad (\text{B6})$$

where $\Delta_L \sigma_{\pi N}$ is the finite-volume correction to the σ -term [100]. The remaining terms reflect the excited states, with diagram (a_1) receiving a contribution from $N\pi$ intermediate states (nucleon and pion having opposite momenta) and from an $N\pi\pi$ state (the nucleon at rest and the two pions carrying momenta $\pm\mathbf{k}$). The $N\pi$ and $N\pi\pi$ states with zero pion momentum vanish due to the prefactor \mathbf{k}^2 . The amplitude of the $N\pi$ contribution is suppressed by $(M_\pi L)^3$ compared to $g_S^{(0)}$, but enhanced by the large coupling of a scalar source to the pion, making it suppressed by only a single chiral order. The last line of Eq. (B5) originates from diagram (b_1). In this case the dominant excited state is $N\pi\pi$, with the two pions at zero momentum. Diagram (g_2) arises from the last term in the square bracket in Eq. (B4). Though formally NLO, this diagram vanishes up to $\mathcal{O}(1/M_N)$ corrections, and thus the topology (g_2) only contributes to N²LO. Similarly, the diagram with the pion emitted by \mathcal{N} and absorbed by $\tilde{\mathcal{N}}$ vanishes at NLO.

At N²LO there are several contributions. They come from loop corrections to the LO (diagrams (a_2), (b_2), and (c_2)) and from diagrams with subleading interactions in the chiral Lagrangian and the scalar source coupling to two pions (diagrams (d_2), (e_2), and (f_2)). Here, diagrams (a_2) and (b_2) are exactly canceled by the N²LO corrections to the 2-point function. This is in contrast to the isovector case, in which they are responsible for the

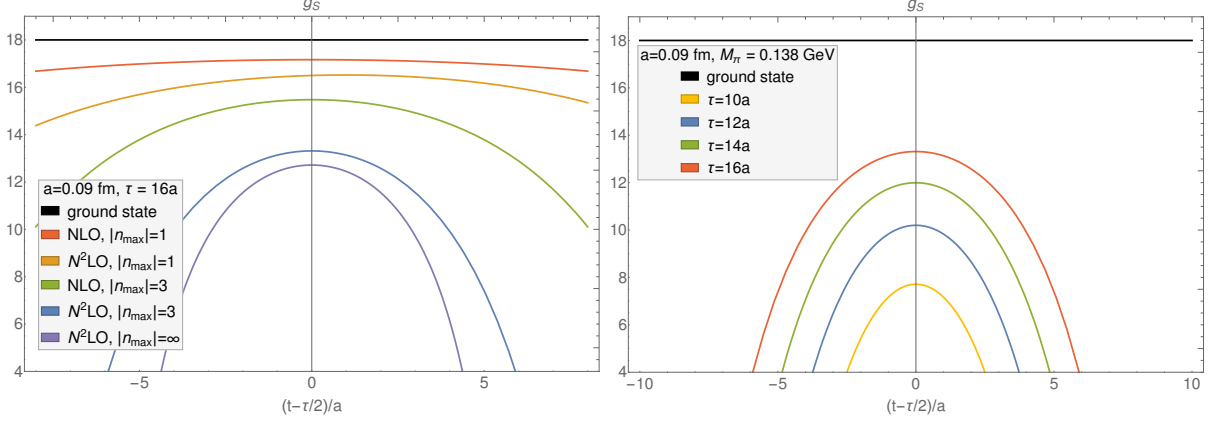


FIG. 5. (Left) Excited-state corrections from different truncations to the isoscalar scalar charge g_S in χ PT. (Right) Estimates for $\mathcal{R}_S(\tau, t)$ from the N^2 LO analysis for the $a09m130$ ensemble, which should be compared to the data in Fig. 2 (and the shape with that of the separate contributions shown in Fig. 6). We assume $g_S = 18$ is the asymptotic value in both cases.

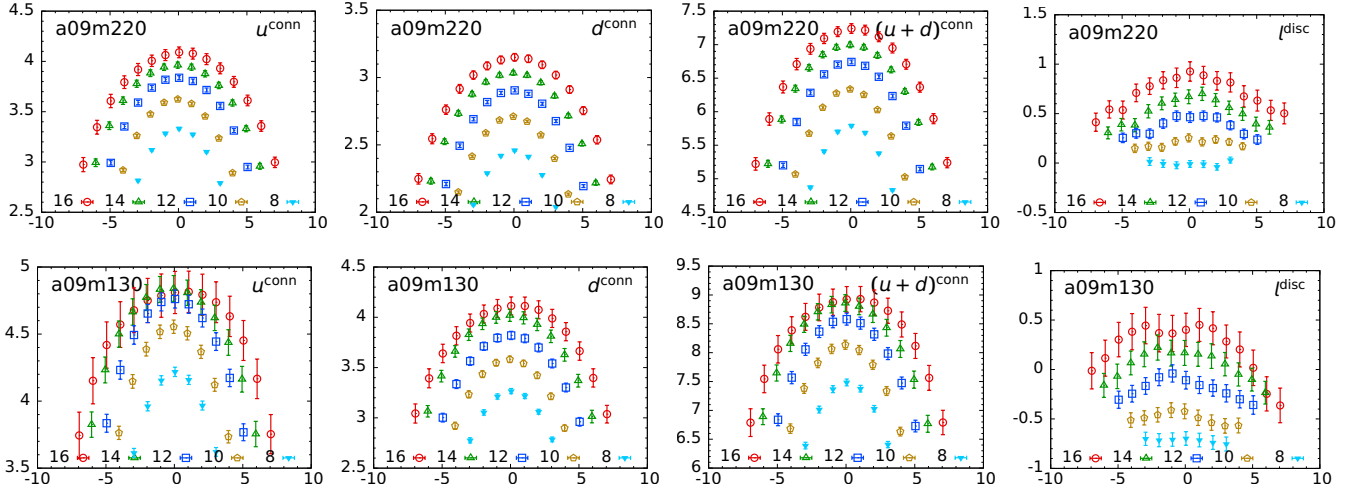


FIG. 6. Data for the ratio $\mathcal{R}_S = C(3pt)/C(2pt)$ for τ/a listed in the label are shown for the u , d , and $(u+d)$ connected, and light quark l disconnected contributions, and plotted versus $(t - \tau/2)/a$ for the $a09m220$ (top) and $a09m130$ (bottom) ensembles.

leading ESC:

$$\mathcal{R}_{\text{isovector}}^{(2)}(\tau, t) = -m_{ud}\tilde{g}_S^{(0)} \frac{g_A^2}{2F_\pi^2} \frac{1}{L^3} \sum_{\mathbf{k}} \frac{\mathbf{k}^2}{E_\pi^3} \times \left[1 - e^{-E_\pi t} - e^{-E_\pi t_B} + e^{-E_\pi \tau} \right]. \quad (\text{B7})$$

This result agrees with the corrections to the isovector scalar charge computed in Ref. [75], once we expand in the limit $M_N \gg |\mathbf{k}|$.

Diagram (c_2) only contributes to the ground state, and diagrams (d_2) and (e_2) are recoil corrections. A first effect of these diagrams is to shift the energy excitation of the $N\pi$ state from E_π to $E_\pi + \tilde{E}_N$. The remaining

recoil corrections are

$$\begin{aligned} \mathcal{R}_{\text{recoil}}^{(2)} = & -\frac{9g_A^2 M_\pi^2}{32M_N F_\pi^2 L^3} \sum_{\mathbf{k}} \frac{(\mathbf{k}^2)^2}{E_\pi^5} \left[1 - \frac{2}{3}e^{-E_\pi t} \right. \\ & - \frac{2}{3}e^{-E_\pi t_B} + \frac{2}{3}e^{-E_\pi \tau} - \frac{1}{6}e^{-2E_\pi t} - \frac{1}{6}e^{-2E_\pi t_B} \Big] \\ & + \frac{3g_A^2 M_\pi^2}{32M_N F_\pi^2 L^3} \sum_{\mathbf{k}} \frac{1}{E_\pi} \left[1 - \frac{1}{2}e^{-2E_\pi t} - \frac{1}{2}e^{-2E_\pi t_B} \right. \\ & \left. + \frac{2\mathbf{k}^2}{E_\pi^2} \left(1 - e^{-E_\pi t} - e^{-E_\pi t_B} + e^{-E_\pi \tau} \right) \right]. \quad (\text{B8}) \end{aligned}$$

Finally, diagram (d_2) receives contributions from the LECs $c_{1,2,3}$, which contribute to πN scattering at NLO

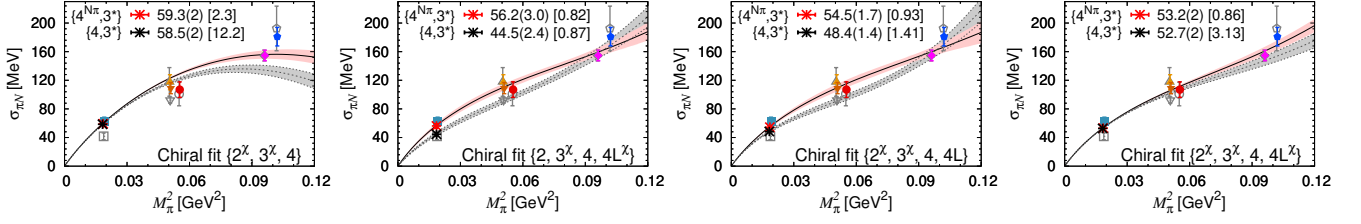


FIG. 7. Chiral fits to the data for the σ -term, $\sigma_{\pi N} = m_{ud} g_S^{u+d}$, from the two ESC strategies $\{4, 3^*\}$ (gray) and $\{4^{N\pi}, 3^*\}$ (color) shown as a function of M_π^2 . The four chiral fits are $\{2^X, 3^X, 4\}$, $\{2, 3^X, 4, 4L^X\}$, $\{2^X, 3^X, 4, 4L\}$, and $\{2^X, 3^X, 4, 4L^X\}$. The result at $M_\pi = 135$ MeV and the $[\chi^2/\text{dof}]$ of the chiral fit for the two ESC strategies are given in the legend.

chiral fit	$\{4, 3^*\}$						$\{4^{N\pi}, 3^*\}$					
	d_2 (GeV $^{-1}$)	d_3 (GeV $^{-2}$)	d_4 (GeV $^{-3}$)	d_{4L} (GeV $^{-3}$)	χ^2_{dof}	$\sigma_{\pi N}$ (MeV)	d_2 (GeV $^{-1}$)	d_3 (GeV $^{-2}$)	d_4 (GeV $^{-3}$)	d_{4L} (GeV $^{-3}$)	χ^2_{dof}	$\sigma_{\pi N}$ (MeV)
χPT	4.44	-8.55	-	11.35	-	-	4.44	-8.55	-	11.35	-	-
$\{2, 3\}$	2.48(29)	-2.8(1.1)	-	-	0.68	38.3(2.8)	3.74(35)	-6.7(1.2)	-	-	1.48	51.6(3.5)
$\{2, 3, 4\}$	3.1(1.2)	-8(10)	10(20)	-	0.82	40.3(4.7)	6.7(1.6)	-31(13)	47(25)	-	0.84	61.6(6.4)
$\{2^X, 3^X, 4\}$	4.44	-8.55	-4.07(71)	-	12.2	58.50(24)	4.44	-8.55	-1.72(64)	-	2.30	59.28(21)
$\{2, 3^X, 4, 4L\}$	3.14(73)	-8.55	11(19)	-0.5(11.7)	0.82	40.4(4.7)	5.57(96)	-8.55	45(23)	26(15)	0.77	61.7(6.3)
$\{2, 3^X, 4, 4L^X\}$	3.86(17)	-8.55	29.6(2.2)	11.35	0.87	44.5(2.4)	4.65(21)	-8.55	21.7(2.4)	11.35	0.82	56.2(3.0)
$\{2^X, 3^X, 4, 4L\}$	4.44	-8.55	42.2(6.3)	19.8(2.7)	1.41	48.4(1.4)	4.44	-8.55	18.5(7.2)	8.9(3.2)	0.93	54.5(1.7)
$\{2^X, 3^X, 4, 4L^X\}$	4.44	-8.55	22.51(71)	11.35	3.13	52.72(24)	4.44	-8.55	23.97(64)	11.35	0.86	53.20(21)

TABLE IV. Chiral fit coefficients with the ansatz $d_2 M_\pi^2 + d_3 M_\pi^3 + d_4 M_\pi^4 + d_{4L} M_\pi^4 \log(M_\pi/M_N)^2$. Here the χPT values for d_i are calculated using Eq. (B10) and with $M_N = 0.939$ GeV, $g_A = 1.276$, $F_\pi = 92.3$ MeV. d_{4L} includes the chiral logarithm in $\bar{l}_3 = -\log M_\pi^2 + \text{finite}$.

in χPT . Including diagram (c_2) , they give

$$\begin{aligned} \mathcal{R}_{c_i}^{(2)} = & -\frac{3M_\pi^2}{4F_\pi^2} \frac{1}{L^3} \sum_{\mathbf{k}} \frac{1}{E_\pi^3} \left((c_2 + 2c_3) E_\pi^2 \right. \\ & \left. + (2c_1 - c_3) M_\pi^2 \right) \left[1 - \frac{1}{2} e^{-2E_\pi t} - \frac{1}{2} e^{-2E_\pi t_B} \right] \\ & + \frac{3M_\pi^2}{F_\pi^2} \frac{1}{L^3} \sum_{\mathbf{k}} \frac{1}{E_\pi} c_1. \end{aligned} \quad (\text{B9})$$

The energy gap in this case is $\approx 2M_\pi$, since $\mathbf{k} = \mathbf{0}$ is allowed. The LECs $c_{1,2,3}$ have been determined most reliably by an analysis of πN scattering using Roy-Steiner equations, matched to χPT in the subthreshold region [32, 33]. We will use the N^3LO values

$$\begin{aligned} c_1 &= -1.11(3) \text{ GeV}^{-1}, & c_2 &= 3.13(3) \text{ GeV}^{-1}, \\ c_3 &= -5.61(6) \text{ GeV}^{-1}, \end{aligned} \quad (\text{B10})$$

which correspond to N^2LO in the scalar form factor. We neglect the N^2LO diagrams with pions emitted by the nucleon source, represented by (g_2) , (h_2) , and (i_2) in Fig. 3, given that for a local source the NLO contribution is already small. Of these diagrams, (g_2) produces N^2LO recoil corrections, (h_2) contains unknown LECs that appear in the expansion of the source, and (i_2) cancels in the ratio between the 2- and 3-point function. While we have assumed local nucleon sources, the relative importance of the diagrams in Fig. 3 depends on the details of the lattice realization of \mathcal{N} . However, the study of the ESC to the scalar charge with smeared nucleon sources

used in realistic lattice simulations is beyond the scope of this work.

In the infinite-volume limit, the ground-state pieces of Eqs. (B5), (B8), and (B9) reproduce the N^2LO expression for the σ -term (in the form given in Ref. [33])

$$\begin{aligned} \sigma_{\pi N} &= m_{ud} \frac{\partial M_N}{\partial m_{ud}} = m_{ud} g_S^{u+d} \quad (\text{B11}) \\ &= -4c_1 M_\pi^2 - \frac{9g_A^2 M_\pi^3}{64\pi F_\pi^2} - \frac{3M_\pi^4}{64\pi^2 F_\pi^2} \left(2 \log \frac{M_\pi^2}{M_N^2} + 1 \right) \\ &\times \left(\frac{g_A^2}{M_N} - 8c_1 + c_2 + 4c_3 \right) \\ &+ 2M_\pi^4 \left\{ e_1 + \frac{3}{128\pi^2 F_\pi^2} \left(c_2 - \frac{2g_A^2}{M_N} \right) + \frac{c_1(\bar{l}_3 - 1)}{16\pi^2 F_\pi^2} \right\}, \end{aligned}$$

except for the LO contribution proportional to $c_1 M_\pi^2$, its quark-mass renormalization proportional to $\bar{l}_3 - 1$, and the N^2LO LEC e_1 , all of which only contribute to the ground state. All other terms in Eq. (B11) can be obtained by replacing the finite-volume sum $1/L^3 \sum_{\mathbf{k}}$ with infinite-volume integrals in Eqs. (B5), (B8), and (B9).

To assess the importance of the $N\pi$ and $N\pi\pi$ contributions we define

$$\delta\sigma_{\pi N}(\tau, t) = \mathcal{R}(\tau, t) - \lim_{t, \tau \rightarrow \infty} \mathcal{R}(\tau, t). \quad (\text{B12})$$

The contributions to $\delta\sigma_{\pi N}$ from the NLO diagrams (including the formally N^2LO correction from \tilde{E}_N) and from the N^2LO diagrams are evaluated in Table III, using the parameters of the $a09m130$ lattice ensemble, for two

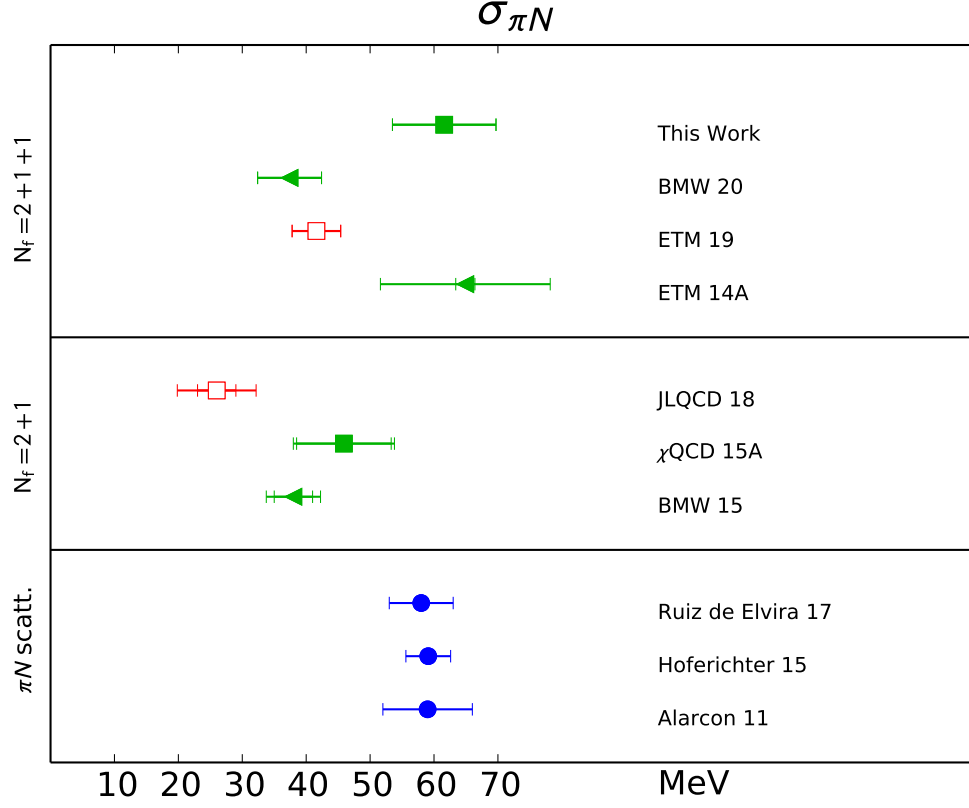


FIG. 8. Results for $\sigma_{\pi N} = m_{ud}g_S^{u+d}$ from 2+1- and 2+1+1-flavor lattice calculations. The BMW 20 result from 1+1+1+1-flavor lattices is listed along with the other 2+1+1-flavor calculations for brevity. Following the FLAG conventions, determinations via the direct approach are indicated by squares and the FH method by triangles. Also, the symbols used for lattice estimates that satisfy the FLAG criteria for inclusion in averages are filled green, and those not included are open red. The references from which lattice results have been taken are: JLQCD 18 [60], χ QCD 15A [57], BMW 15 [56], ETM 14A [63], ETM 19 [61], and BMW 20 [62]. Phenomenological estimates using πN scattering data (blue filled circles) are from Alarcon 11 [28], Hoferichter 15 [31], and Ruiz de Elvira 17 [37].

choices of source-sink separation, $\tau = 16a$ and $\tau = 12a$. We list separately the corrections from diagram (a_1) and (b_1) in Fig. 3, as the first is dominated by $N\pi$ excited states, the second by $N\pi\pi$. Similarly, the N^2 LO corrections from the diagrams proportional to the LECs $c_{1,2,3}$ receive contributions from $N\pi\pi$ states, while the recoil corrections in Eq. (B8) are dominated by $N\pi$. From Table III we see that $\mathcal{R}^{(1)}$ and $\mathcal{R}^{(2)}$ are of similar size and the most important contributions come from diagram (a_1) and from Eq. (B9). The nucleon source and recoil contributions are substantially smaller.

We also note that the ESC is amplified by the presence of several states close in energy. We can see this in the left panel of Fig. 5, where the red and orange curves denote the NLO and N^2 LO corrections, including states up to $|\mathbf{n}_{\max}| = 1$, while the green and blue curves include states up to $|\mathbf{n}_{\max}| = 3$. In the continuum, the effect of the entire tower of excited states can be resummed, with the result shown in the last line of Table III and by the purple line in Fig. 5. The comparison to the different $|\mathbf{n}_{\max}|$ values indicates the degree of convergence, which is ulti-

mately determined by t and τ via the exponential suppression of the continuum integrals. Indeed, we see that for $\tau = 16a$ the corrections at $t = 8a$ beyond $|\mathbf{n}_{\max}| = 3$ are around 10%, but twice as large for $\tau = 12a$, $t = 6a$. Away from $t \sim \tau/2$, the integrals become increasingly dominated by large-momentum modes, leading to the eventual breakdown of the chiral expansion. For this reason, the expansion becomes less reliable for small and large t , which explains why the functional form predicted by χ PT, see the right panel of Fig. 5, suggests a faster decrease towards the edges than observed in the lattice data, see Figs. 2 and 6. In the center, however, the EFT expansion should be reliable, in particular for the $\tau = 16a$ variant, which leads to the conclusion that NLO and N^2 LO contributions can each lead to a reduction of $\sigma_{\pi N}$ at the level of 10 MeV. Note that Fig. 6 shows the behavior versus t and τ for the individual contributions, i.e., insertions on the u , the d , and the disconnected loop l .

While in Table III and Fig. 5 we focused on the ensemble with the lightest pion mass, we find good agreement between the χ PT expectations and the fits in Fig. 2

also for the remaining ensembles. For example, with the parameters of the $a09m220$ ensemble, χ PT predicts the difference between the lattice data and the extrapolated value of g_S to be 3 at $t = \tau/2 = 8a$, in good agreement with the first panel in the second row of Fig. 2. Similarly, for the $a06m220$ and $a06m310$ ensembles we obtain that g_S is shifted by 2.8 and 1.6, at $t = \tau/2 = 12a$.

Finally, using Eq. (B11), we have carried out the following chiral fits to the lattice data: $\{2, 3\}$, $\{2^\chi, 3^\chi, 4\}$, $\{2, 3^\chi, 4, 4L^\chi\}$, $\{2^\chi, 3^\chi, 4, 4L\}$, and $\{2^\chi, 3^\chi, 4, 4L^\chi\}$, in addition to the fits $\{2, 3, 4\}$, $\{2, 3^\chi, 4, 4L\}$ already shown in Fig. 4. Four of these additional fits are shown in Fig. 7, with resulting fit parameters given in Table IV. We see that for the $\{4^{N\pi}, 3^*\}$ strategy all fit variants lead to parameters that agree with the χ PT prediction (including evidence for the nonanalytic M_π^3 term from the $\{2, 3\}$ and $\{2, 3, 4\}$ fits), with changes in $\sigma_{\pi N}$ consistent with the uncertainty assigned to the least constrained fits ($\{2, 3, 4\}$ and $\{2, 3^\chi, 4, 4L\}$), whose average we quoted as our central result. Even in the most-constrained case $\{2^\chi, 3^\chi, 4, 4L^\chi\}$ a good fit of the data is obtained, in marked contrast to the $\{4, 3^*\}$ strategy, in which case the χ^2/dof becomes unacceptable when imposing the maximum amount of chiral constraints.

We end this appendix by pointing out a subtlety. We

have used the lowest-order (linear) relation between M_π^2 and $1/2\kappa$ to get m_{ud}^{bare} as we have ensembles at only two values of M_π at each a . Higher-order corrections give the LEC \bar{l}_3 term in Eq. (B11). Removing it changes the χ PT prediction of the d_{4L} term in Table IV from 11.35 to 9.70, however, the results of the $\{2, 3^\chi, 4, 4L^\chi\}$ and $\{2^\chi, 3^\chi, 4, 4L^\chi\}$ fits do not change significantly.

Appendix C: Update of FLAG 2019 Results for $\sigma_{\pi N}$

Figure 8 gives an update on the summary of results for $\sigma_{\pi N}$ presented in the FLAG review 2019 [64] using the same notation. We focus on a comparison of results from lattice QCD and those from πN scattering data. For the lattice data, we retain only the 2+1 and 2+1+1 (and 1+1+1+1) flavor results obtained since 2015, see Refs. [54, 55, 58, 59, 101–107] for other determinations included in the FLAG review. Moreover, Fig. 8 does not include results from calculations that analyze more than one lattice data set within the FH approach [108–117], or results that use a mixture of lattice QCD and phenomenological analyses [118]. Most of the recent lattice results are clustered around $\sigma_{\pi N} \approx 40 \text{ MeV}$, while the phenomenological estimates are at $\sigma_{\pi N} \approx 60 \text{ MeV}$, as is our result with $N\pi/N\pi\pi$ included when removing ESC.

-
- [1] H. Hellman, *Einführung in die Quantenchemie* (Franz Deuticke, Leipzig und Wein, 1937).
 - [2] R. P. Feynman, Phys. Rev. **56**, 340 (1939).
 - [3] J. Gasser and A. Zepeda, Nucl. Phys. B **174**, 445 (1980).
 - [4] A. Bottino, F. Donato, N. Fornengo, and S. Scopel, Astropart. Phys. **13**, 215 (2000), arXiv:hep-ph/9909228.
 - [5] A. Bottino, F. Donato, N. Fornengo, and S. Scopel, Astropart. Phys. **18**, 205 (2002), arXiv:hep-ph/0111229.
 - [6] J. R. Ellis, K. A. Olive, and C. Savage, Phys. Rev. D **77**, 065026 (2008), arXiv:0801.3656 [hep-ph].
 - [7] A. Crivellin, M. Hoferichter, and M. Procura, Phys. Rev. D **89**, 054021 (2014), arXiv:1312.4951 [hep-ph].
 - [8] M. Hoferichter, P. Klos, J. Menéndez, and A. Schwenk, Phys. Rev. Lett. **119**, 181803 (2017), arXiv:1708.02245 [hep-ph].
 - [9] V. Cirigliano, R. Kitano, Y. Okada, and P. Tuzon, Phys. Rev. D **80**, 013002 (2009), arXiv:0904.0957 [hep-ph].
 - [10] A. Crivellin, M. Hoferichter, and M. Procura, Phys. Rev. D **89**, 093024 (2014), arXiv:1404.7134 [hep-ph].
 - [11] J. Engel, M. J. Ramsey-Musolf, and U. van Kolck, Prog. Part. Nucl. Phys. **71**, 21 (2013), arXiv:1303.2371 [nucl-th].
 - [12] J. de Vries and U.-G. Meißner, Int. J. Mod. Phys. E **25**, 1641008 (2016), arXiv:1509.07331 [hep-ph].
 - [13] J. de Vries, E. Mereghetti, C.-Y. Seng, and A. Walker-Loud, Phys. Lett. B **766**, 254 (2017), arXiv:1612.01567 [hep-lat].
 - [14] N. Yamanaka, B. K. Sahoo, N. Yoshinaga, T. Sato, K. Asahi, and B. P. Das, Eur. Phys. J. A **53**, 54 (2017), arXiv:1703.01570 [hep-ph].
 - [15] T. P. Cheng and R. F. Dashen, Phys. Rev. Lett. **26**, 594 (1971).
 - [16] L. S. Brown, W. J. Pardee, and R. D. Peccei, Phys. Rev. D **4**, 2801 (1971).
 - [17] V. Bernard, N. Kaiser, and U.-G. Meißner, Phys. Lett. B **389**, 144 (1996), arXiv:hep-ph/9607245.
 - [18] T. Becher and H. Leutwyler, JHEP **06**, 017 (2001), arXiv:hep-ph/0103263.
 - [19] J. Gasser, H. Leutwyler, M. P. Locher, and M. E. Sainio, Phys. Lett. B **213**, 85 (1988).
 - [20] J. Gasser, H. Leutwyler, and M. E. Sainio, Phys. Lett. B **253**, 252 (1991).
 - [21] J. Gasser, H. Leutwyler, and M. E. Sainio, Phys. Lett. B **253**, 260 (1991).
 - [22] R. Koch and E. Pietarinen, Nucl. Phys. A **336**, 331 (1980).
 - [23] G. Höhler, *Methods and Results of Phenomenological Analyses*, edited by H. Schopper, Landolt-Boernstein - Group I Elementary Particles, Nuclei and Atoms, Vol. 9b2 (Springer-Verlag Berlin, Heidelberg, 1983).
 - [24] R. A. Arndt, W. J. Briscoe, I. I. Strakovsky, and R. L. Workman, Phys. Rev. C **74**, 045205 (2006), arXiv:nucl-th/0605082.
 - [25] R. L. Workman, R. A. Arndt, W. J. Briscoe, M. W. Paris, and I. I. Strakovsky, Phys. Rev. C **86**, 035202 (2012), arXiv:1204.2277 [hep-ph].
 - [26] M. M. Pavan, I. I. Strakovsky, R. L. Workman, and R. A. Arndt, PiN Newslett. **16**, 110 (2002), arXiv:hep-ph/0111066.
 - [27] N. Fettes and U.-G. Meißner, Nucl. Phys. A **676**, 311 (2000), arXiv:hep-ph/0002162.

- [28] J. M. Alarcón, J. Martin Camalich, and J. A. Oller, Phys. Rev. D **85**, 051503 (2012), arXiv:1110.3797 [hep-ph].
- [29] C. Ditsche, M. Hoferichter, B. Kubis, and U.-G. Meißner, JHEP **06**, 043 (2012), arXiv:1203.4758 [hep-ph].
- [30] M. Hoferichter, C. Ditsche, B. Kubis, and U.-G. Meißner, JHEP **06**, 063 (2012), arXiv:1204.6251 [hep-ph].
- [31] M. Hoferichter, J. Ruiz de Elvira, B. Kubis, and U.-G. Meißner, Phys. Rev. Lett. **115**, 092301 (2015), arXiv:1506.04142 [hep-ph].
- [32] M. Hoferichter, J. Ruiz de Elvira, B. Kubis, and U.-G. Meißner, Phys. Rev. Lett. **115**, 192301 (2015), arXiv:1507.07552 [nucl-th].
- [33] M. Hoferichter, J. Ruiz de Elvira, B. Kubis, and U.-G. Meißner, Phys. Rept. **625**, 1 (2016), arXiv:1510.06039 [hep-ph].
- [34] M. Hoferichter, J. Ruiz de Elvira, B. Kubis, and U.-G. Meißner, Phys. Lett. B **760**, 74 (2016), arXiv:1602.07688 [hep-lat].
- [35] M. Hoferichter, B. Kubis, J. Ruiz de Elvira, H.-W. Hammer, and U.-G. Meißner, Eur. Phys. J. A **52**, 331 (2016), arXiv:1609.06722 [hep-ph].
- [36] D. Siemens, J. Ruiz de Elvira, E. Epelbaum, M. Hoferichter, H. Krebs, B. Kubis, and U.-G. Meißner, Phys. Lett. B **770**, 27 (2017), arXiv:1610.08978 [nucl-th].
- [37] J. Ruiz de Elvira, M. Hoferichter, B. Kubis, and U.-G. Meißner, J. Phys. G **45**, 024001 (2018), arXiv:1706.01465 [hep-ph].
- [38] T. Strauch *et al.*, Eur. Phys. J. A **47**, 88 (2011), arXiv:1011.2415 [nucl-ex].
- [39] M. Hennebach *et al.*, Eur. Phys. J. A **50**, 190 (2014), [Erratum: Eur. Phys. J. A **55**, 24 (2019)], arXiv:1406.6525 [nucl-ex].
- [40] A. Hirtl *et al.*, Eur. Phys. J. A **57**, 70 (2021).
- [41] V. Baru, C. Hanhart, M. Hoferichter, B. Kubis, A. Nogga, and D. R. Phillips, Phys. Lett. B **694**, 473 (2011), arXiv:1003.4444 [nucl-th].
- [42] V. Baru, C. Hanhart, M. Hoferichter, B. Kubis, A. Nogga, and D. R. Phillips, Nucl. Phys. A **872**, 69 (2011), arXiv:1107.5509 [nucl-th].
- [43] J. Gasser, M. A. Ivanov, E. Lipartia, M. Mojžiš, and A. Rusetsky, Eur. Phys. J. C **26**, 13 (2002), arXiv:hep-ph/0206068.
- [44] M. Hoferichter, B. Kubis, and U.-G. Meißner, Phys. Lett. **B678**, 65 (2009), arXiv:0903.3890 [hep-ph].
- [45] M. Hoferichter, B. Kubis, and U.-G. Meißner, Nucl. Phys. A **833**, 18 (2010), arXiv:0909.4390 [hep-ph].
- [46] M. Hoferichter, V. Baru, C. Hanhart, B. Kubis, A. Nogga, and D. R. Phillips, PoS **CD12**, 093 (2013), arXiv:1211.1145 [nucl-th].
- [47] J. T. Brack *et al.*, Phys. Rev. C **41**, 2202 (1990).
- [48] C. Joram, M. Metzler, J. Jaki, W. Kluge, H. Matthäy, R. Wieser, B. M. Barnett, H. Clement, S. Krell, and G. J. Wagner, Phys. Rev. C **51**, 2144 (1995).
- [49] H. Denz *et al.*, Phys. Lett. B **633**, 209 (2006), arXiv:nucl-ex/0512006.
- [50] E. Frlež *et al.*, Phys. Rev. C **57**, 3144 (1998), arXiv:hep-ex/9712024.
- [51] L. D. Isenhowe *et al.*, PiN Newslett. **15**, 292 (1999).
- [52] Y. Jia, T. P. Gorringe, M. D. Hasinoff, M. A. Kovash, M. Ojha, M. M. Pavan, S. Tripathi, and P. A. Żołnierczuk, Phys. Rev. Lett. **101**, 102301 (2008), arXiv:0804.1531 [nucl-ex].
- [53] D. Mekterović *et al.* (Crystal Ball), Phys. Rev. C **80**, 055207 (2009), arXiv:0908.3845 [hep-ex].
- [54] S. Dürr *et al.* (BMWc), Phys. Rev. D **85**, 014509 (2012), [Erratum: Phys. Rev. D **93**, 039905 (2016)], arXiv:1109.4265 [hep-lat].
- [55] G. S. Bali *et al.* (QCDSF), Nucl. Phys. B **866**, 1 (2013), arXiv:1206.7034 [hep-lat].
- [56] S. Dürr *et al.* (BMWc), Phys. Rev. Lett. **116**, 172001 (2016), arXiv:1510.08013 [hep-lat].
- [57] Y.-B. Yang, A. Alexandru, T. Draper, J. Liang, and K.-F. Liu (χ QCD), Phys. Rev. D **94**, 054503 (2016), arXiv:1511.09089 [hep-lat].
- [58] A. Abdel-Rehim, C. Alexandrou, M. Constantinou, K. Hadjiyiannakou, K. Jansen, C. Kallidonis, G. Koutsou, and A. Vaquero Avilés-Casco (ETM), Phys. Rev. Lett. **116**, 252001 (2016), arXiv:1601.01624 [hep-lat].
- [59] G. S. Bali, S. Collins, D. Richtmann, A. Schäfer, W. Söldner, and A. Sternbeck (RQCD), Phys. Rev. D **93**, 094504 (2016), arXiv:1603.00827 [hep-lat].
- [60] N. Yamanaka, S. Hashimoto, T. Kaneko, and H. Ohki (JLQCD), Phys. Rev. D **98**, 054516 (2018), arXiv:1805.10507 [hep-lat].
- [61] C. Alexandrou, S. Bacchio, M. Constantinou, J. Finkenrath, K. Hadjiyiannakou, K. Jansen, G. Koutsou, and A. Vaquero Avilés-Casco (ETM), Phys. Rev. D **102**, 054517 (2020), arXiv:1909.00485 [hep-lat].
- [62] S. Borsanyi, Z. Fodor, C. Hoelbling, L. Lellouch, K. K. Szabo, C. Torrero, and L. Varnhorst (BMWc), (2020), arXiv:2007.03319 [hep-lat].
- [63] C. Alexandrou, V. Drach, K. Jansen, C. Kallidonis, and G. Koutsou, Phys. Rev. D **90**, 074501 (2014), arXiv:1406.4310 [hep-lat].
- [64] S. Aoki *et al.* (Flavour Lattice Averaging Group), Eur. Phys. J. C **80**, 113 (2020), arXiv:1902.08191 [hep-lat].
- [65] E. E. Jenkins and A. V. Manohar, Phys. Lett. B **255**, 558 (1991).
- [66] V. Bernard, N. Kaiser, J. Kambor, and U.-G. Meißner, Nucl. Phys. B **388**, 315 (1992).
- [67] E. Follana *et al.* (HPQCD, UKQCD), Phys. Rev. D **75**, 054502 (2007), arXiv:hep-lat/0610092 [hep-lat].
- [68] A. Bazavov *et al.* (MILC), Phys. Rev. D **87**, 054505 (2013), arXiv:1212.4768 [hep-lat].
- [69] T. Bhattacharya, V. Cirigliano, S. Cohen, R. Gupta, A. Joseph, H.-W. Lin, and B. Yoon (PNDME), Phys. Rev. D **92**, 094511 (2015), arXiv:1506.06411 [hep-lat].
- [70] R. Gupta, Y.-C. Jang, B. Yoon, H.-W. Lin, V. Cirigliano, and T. Bhattacharya, Phys. Rev. D **98**, 034503 (2018), arXiv:1806.09006 [hep-lat].
- [71] Y.-C. Jang, R. Gupta, B. Yoon, and T. Bhattacharya, Phys. Rev. Lett. **124**, 072002 (2020), arXiv:1905.06470 [hep-lat].
- [72] S. Park, R. Gupta, B. Yoon, S. Mondal, T. Bhattacharya, Y.-C. Jang, B. Joó, and F. Winter (Nucleon Matrix Elements), (2021), arXiv:2103.05599 [hep-lat].
- [73] O. Bär, Phys. Rev. D **92**, 074504 (2015), arXiv:1503.03649 [hep-lat].
- [74] B. C. Tiburzi, Phys. Rev. D **91**, 094510 (2015), arXiv:1503.06329 [hep-lat].
- [75] O. Bär, Phys. Rev. D **94**, 054505 (2016), arXiv:1606.09385 [hep-lat].
- [76] O. Bär, Phys. Rev. D **95**, 034506 (2017), arXiv:1612.08336 [hep-lat].

- [77] O. Bär, Phys. Rev. D **97**, 094507 (2018), arXiv:1802.10442 [hep-lat].
- [78] O. Bär, Phys. Rev. D **99**, 054506 (2019), arXiv:1812.09191 [hep-lat].
- [79] O. Bär, Phys. Rev. D **100**, 054507 (2019), arXiv:1906.03652 [hep-lat].
- [80] O. Bär and H. Čolić, (2021), arXiv:2104.00329 [hep-lat].
- [81] V. Dmitrašinović, A. Hosaka, and K. Nagata, Mod. Phys. Lett. A **25**, 233 (2010), arXiv:0912.2372 [hep-ph].
- [82] H.-W. Lin *et al.*, Prog. Part. Nucl. Phys. **100**, 107 (2018), arXiv:1711.07916 [hep-ph].
- [83] R. G. Edwards and B. Joó (SciDAC, LHPC, UKQCD), Nucl. Phys. Proc. Suppl. **140**, 832 (2005), arXiv:hep-lat/0409003 [hep-lat].
- [84] G. S. Bali, S. Collins, and A. Schäfer, Comput. Phys. Commun. **181**, 1570 (2010), arXiv:0910.3970 [hep-lat].
- [85] T. Blum, T. Izubuchi, and E. Shintani, Phys. Rev. D **88**, 094503 (2013), arXiv:1208.4349 [hep-lat].
- [86] S. Gusken, U. Low, K. H. Mutter, R. Sommer, A. Patel, and K. Schilling, Phys. Lett. B **227**, 266 (1989).
- [87] J. Gasser, M. E. Sainio, and A. Švarc, Nucl. Phys. B **307**, 779 (1988).
- [88] V. Bernard, N. Kaiser, and U.-G. Meißner, Int. J. Mod. Phys. E **4**, 193 (1995), arXiv:hep-ph/9501384 [hep-ph].
- [89] B. Borasoy and U.-G. Meißner, Annals Phys. **254**, 192 (1997), arXiv:hep-ph/9607432.
- [90] U.-G. Meißner and S. Steininger, Phys. Lett. B **419**, 403 (1998), arXiv:hep-ph/9709453.
- [91] S. Steininger, U.-G. Meißner, and N. Fettes, JHEP **09**, 008 (1998), arXiv:hep-ph/9808280.
- [92] J. Kambor and M. Mojžiš, JHEP **04**, 031 (1999), arXiv:hep-ph/9901235.
- [93] J. A. McGovern and M. C. Birse, Phys. Lett. B **446**, 300 (1999), arXiv:hep-ph/9807384.
- [94] T. Becher and H. Leutwyler, Eur. Phys. J. C **9**, 643 (1999), arXiv:hep-ph/9901384.
- [95] J. A. McGovern and M. C. Birse, Phys. Rev. D **74**, 097501 (2006), arXiv:hep-lat/0608002.
- [96] M. R. Schindler, D. Djukanovic, J. Gegelia, and S. Scherer, Phys. Lett. B **649**, 390 (2007), arXiv:hep-ph/0612164.
- [97] M. R. Schindler, D. Djukanovic, J. Gegelia, and S. Scherer, Nucl. Phys. A **803**, 68 (2008), [Erratum: Nucl. Phys. A **1010**, 122175 (2021)], arXiv:0707.4296 [hep-ph].
- [98] G. Colangelo and S. Dürr, Eur. Phys. J. C **33**, 543 (2004), arXiv:hep-lat/0311023.
- [99] P. A. Zyla *et al.* (Particle Data Group), PTEP **2020**, 083C01 (2020).
- [100] S. R. Beane, Phys. Rev. D **70**, 034507 (2004), arXiv:hep-lat/0403015.
- [101] H. Ohki, H. Fukaya, S. Hashimoto, T. Kaneko, H. Matsufuru, J. Noaki, T. Onogi, E. Shintani, and N. Yamada, Phys. Rev. D **78**, 054502 (2008), arXiv:0806.4744 [hep-lat].
- [102] K. I. Ishikawa *et al.* (PACS-CS), Phys. Rev. D **80**, 054502 (2009), arXiv:0905.0962 [hep-lat].
- [103] R. Horsley, Y. Nakamura, H. Perlt, D. Pleiter, P. E. L. Rakow, G. Schierholz, A. Schiller, H. Stuben, F. Winter, and J. M. Zanotti (QCDSF-UKQCD), Phys. Rev. D **85**, 034506 (2012), arXiv:1110.4971 [hep-lat].
- [104] J. Martin Camalich, L. S. Geng, and M. J. Vicente Vacas, Phys. Rev. D **82**, 074504 (2010), arXiv:1003.1929 [hep-lat].
- [105] P. E. Shanahan, A. W. Thomas, and R. D. Young, Phys. Rev. D **87**, 074503 (2013), arXiv:1205.5365 [nucl-th].
- [106] H. Ohki, K. Takeda, S. Aoki, S. Hashimoto, T. Kaneko, H. Matsufuru, J. Noaki, and T. Onogi (JLQCD), Phys. Rev. D **87**, 034509 (2013), arXiv:1208.4185 [hep-lat].
- [107] P. Junnarkar and A. Walker-Loud, Phys. Rev. D **87**, 114510 (2013), arXiv:1301.1114 [hep-lat].
- [108] M. Procura, B. U. Musch, T. Wollenweber, T. R. Hemmert, and W. Weise, Phys. Rev. D **73**, 114510 (2006), arXiv:hep-lat/0603001.
- [109] R. D. Young and A. W. Thomas, Phys. Rev. D **81**, 014503 (2010), arXiv:0901.3310 [hep-lat].
- [110] X. L. Ren, L. S. Geng, J. Martin Camalich, J. Meng, and H. Toki, JHEP **12**, 073 (2012), arXiv:1209.3641 [nucl-th].
- [111] L. Alvarez-Ruso, T. Ledwig, J. Martin Camalich, and M. J. Vicente Vacas, Phys. Rev. D **88**, 054507 (2013), arXiv:1304.0483 [hep-ph].
- [112] M. F. M. Lutz, R. Bavontaweepanya, C. Kobdaj, and K. Schwarz, Phys. Rev. D **90**, 054505 (2014), arXiv:1401.7805 [hep-lat].
- [113] X.-L. Ren, L.-S. Geng, and J. Meng, Phys. Rev. D **91**, 051502 (2015), arXiv:1404.4799 [hep-ph].
- [114] X.-L. Ren, L. Alvarez-Ruso, L.-S. Geng, T. Ledwig, J. Meng, and M. J. Vicente Vacas, Phys. Lett. B **766**, 325 (2017), arXiv:1606.03820 [nucl-th].
- [115] C. Alexandrou and C. Kallidonis, Phys. Rev. D **96**, 034511 (2017), arXiv:1704.02647 [hep-lat].
- [116] X.-L. Ren, X.-Z. Ling, and L.-S. Geng, Phys. Lett. B **783**, 7 (2018), arXiv:1710.07164 [hep-ph].
- [117] M. F. M. Lutz, Y. Heo, and X.-Y. Guo, Nucl. Phys. A **977**, 146 (2018), arXiv:1801.06417 [hep-lat].
- [118] Y.-H. Chen, D.-L. Yao, and H. Q. Zheng, Phys. Rev. D **87**, 054019 (2013), arXiv:1212.1893 [hep-ph].